

## Coherent optical control of quantum Hall edge states

Ashutosh Singh,<sup>1,\*</sup> Maria Sebastian<sup>1</sup>,<sup>✉</sup> Mikhail Tokman,<sup>2</sup> and Alexey Belyanin<sup>1,†</sup>

<sup>1</sup>*Department of Physics and Astronomy, Texas A&M University, College Station, Texas 77843, USA*

<sup>2</sup>*Department of Electrical and Electronic Engineering and Schlesinger Knowledge Center for Compact Accelerators and Radiation Sources, Ariel University, 40700 Ariel*



(Received 17 April 2024; revised 7 July 2024; accepted 17 July 2024; published 2 August 2024)

Current-carrying chiral edge states in quantum Hall systems exhibit fascinating properties typically studied using electron spectroscopy and interferometry. Here we demonstrate that electron occupation, current, and coherence in the chiral edge states can be selectively probed and controlled by low-energy electromagnetic radiation in the microwave to infrared range, without affecting electron states in the bulk or disrupting the quantum Hall effect conditions within the sample. Both linear and nonlinear optical controls are feasible due to the inevitable violation of adiabaticity and inversion symmetry breaking for electron states near the edge. This opens up new pathways for frequency- and polarization-selective spectroscopy and the control of individual edge states.

DOI: [10.1103/PhysRevB.110.085405](https://doi.org/10.1103/PhysRevB.110.085405)

### I. INTRODUCTION

The Quantum Hall (QH) effect is one of the most studied phenomena in condensed matter physics [1], with far-reaching applications across numerous fields. One of the most important insights in the QH effect physics is the intricate relationship between the electron states in the insulating bulk of the sample and the current-carrying chiral edge states [2,3] which have been extensively studied with real-space imaging and momentum-resolved electron spectroscopy [4–9]. Furthermore, the coherence of unidirectional electron transport in QH edge states has driven a massive amount of research in QH edge state interferometry. Various types of electron interferometers have been implemented, both in conventional semiconductor quantum wells and in graphene samples, and for both integer and fractional statistics of carriers [10–22].

Microwave and terahertz optical spectroscopy of Landau-quantized electron states in two-dimensional (2D) electron gas is yet another vast area of research. However, its application to probing electron states under QH effect conditions poses significant challenges. Resonant optical transitions between bulk Landau levels (LLs) create nonequilibrium carrier population, thereby allowing for nonzero bulk DC conductivity across the sample. As was argued in Ref. [23], even vacuum cavity fields under the ultra-strong coupling conditions could break the topological protection of the integer QH effect and destroy some of the high quantum number plateaus. Of course the modification of the magnetotransport in the QH samples by sufficiently strong resonant microwave or terahertz fields is an exciting research topic in its own right; see, for example, extensive work dedicated to microwave-induced resistance oscillations (MIRO) and associated zero-resistance states

(ZRS), as reviewed in [24,25] and some of the recent papers [26,27].

In this paper we demonstrate that optical spectroscopy and even coherent optical control of the QH edge states are still possible and can be in fact highly effective without disrupting the QH effect conditions in the bulk. The key physical reason behind this lies in the fact that the optical transitions between electron states near the sample boundary (within a few magnetic lengths from the edge) have significantly different transition energies and polarization selection rules compared to the bulk of the sample. This enables highly selective excitation of a given 1D edge channel with single quasiparticle sensitivity without disturbing the rest of the sample.

Furthermore, inversion symmetry breaking near the sample boundary (as illustrated by highly asymmetric wave functions in the Supplemental Material [28]) enables strong second-order optical nonlinearity in the electric dipole approximation, resulting in efficient optical rectification of incident radiation and direct optical driving of a quasi-DC current in edge states. These qualitative features are illustrated in Figs. 1 and 2, with more quantitative discussion provided in the subsequent sections.

The high spatiotemporal and energy selectivity of optical excitations of chiral edge states not only makes it a sensitive spectroscopy tool complementary to electron transport measurements but also enables coherent control of individual edge channels in QH interferometers, endowing them with new optoelectronic functionality. Further enhancement in selectivity could be possible with near-field tip-enhanced optical microscopy as opposed to the far-field illumination sketched in Fig. 1. Therefore, we anticipate that our paper will stimulate further collaboration between optical and QH effect communities.

In this paper, we focus on the integer QH effect in semiconductor quantum well samples with parabolic electron dispersion. The graphene edge states offer a greater variety

\*Contact author: [asingh.n19@gmail.com](mailto:asingh.n19@gmail.com)

†Contact author: [belyanin@tamu.edu](mailto:belyanin@tamu.edu)

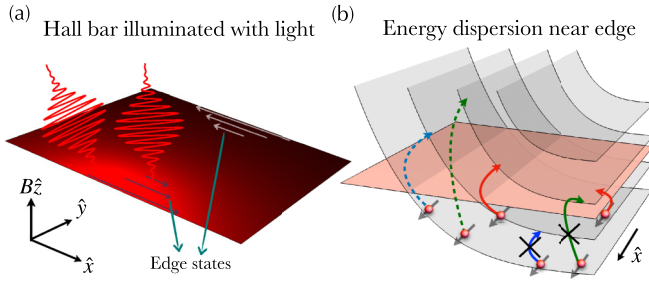


FIG. 1. (a) Photons interacting with electrons moving near one of the edges of a sample which is subjected to a quantizing magnetic field. (b) Near the edge of the sample, energies and wave functions of the electrons are modified in such a way that new channels open up for the absorption of photons or nonlinear optical rectification. Dipole-forbidden (solid green) and Pauli-blocked (solid blue) channels deep in the bulk become active for electrons moving near the edge (marked as dashed green and solid red, respectively).

of optical transitions due to two kinds of edge terminations and will be considered elsewhere, as well as the edge states with fractional statistics of carriers.

The structure of the paper is as follows: In Sec. II, we provide both asymptotic and exact numerical solutions for electron eigenstates and eigenenergies in the presence of an edge treated as a hard-wall boundary, which maximizes nonadiabatic effects. We also calculate dipole matrix elements of the optical transitions between both bulk and edge states.

In Sec. III we compute the single-photon absorption probability for a quantized optical field and derive the 2D absorbance spectra which reveal sharp characteristic peaks at high frequencies that are entirely due to nonadiabatic edge states. Section IV demonstrates various optical mechanisms contributing to direct current (DC) generation through nonlinear rectification of incident radiation. We calculate the second-order nonlinear DC current which exists in the electric dipole approximation solely due to inversion symmetry breaking near the edge. We also evaluate the DC current due to optical rectification beyond the electric dipole approximation, which exists due to the optical field gradient across the sample. It is worth noting that one of the theory proposals to explain MIRO-ZRS phenomena involved a ponderomotive

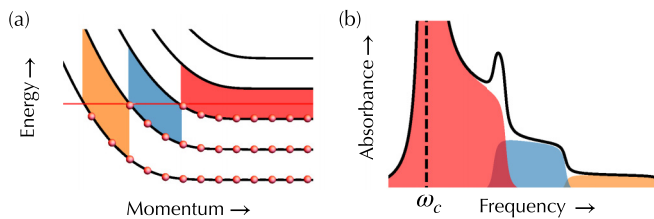


FIG. 2. (a) The plots of eigenenergies as a function of momentum  $k$ . Electron states in shaded regions contribute to photon absorption for a given Fermi level shown with a red horizontal line. (b) The absorbance spectrum. Absorption due to the edge states appears at frequencies higher than the bulk cyclotron resonance frequency  $\omega_c$ . The shaded colored regions under the black curve show the contributions of individual transitions between the neighboring LLs, with matching colors between (a) and (b).

force acting on the edge electrons due to strong optical field gradients near metallic contacts [29], assuming classical electron motion and the adiabatic limit.

Finally, the Appendix summarizes results for electron eigenstates in the adiabatic approximation, derives the electron density flux for an arbitrary electric potential, and gives the list of second-order nonlinear density matrix elements contributing to the rectification current.

## II. CHIRAL EDGE STATES CLOSE TO THE BOUNDARY

Consider a QH system with electrons constrained to the  $x, y$  plane in a quantizing magnetic field  $B$  along  $z$ -axis described by the vector potential  $\vec{A} = -yB\hat{x}$ . Near the boundary in  $y$  direction located at  $y = 0$ , the electron states experience the edge potential  $\Phi(y)$ , so that the Schrödinger equation for a wave function of the form  $\psi_k(x, y) \sim e^{ikx}\chi(y)$  becomes

$$\frac{\partial^2 \chi}{\partial y^2} + \frac{2m}{\hbar^2} \left[ E + e\Phi(y) - \frac{1}{2}m\omega_c^2(y - y_k)^2 \right] \chi(y) = 0, \quad (1)$$

where  $m$  is the electron mass,  $E$  is the energy eigenvalue,  $\omega_c = eB/(mc)$  is the cyclotron frequency,  $y_k = k\ell_c^2$  is the position of the center of the cyclotron oscillator, and  $\ell_c^2 = c\hbar/(eB)$  is the magnetic length.

In the adiabatic approximation which is usually invoked when discussing the edge states (see Appendix A),  $\Phi(y)$  is considered such a slow function of  $y$  that its change over the magnetic length scale is neglected. In this case, while the energies of the LLs increase towards the edge, the energy separation between them does not change and the dipole matrix elements of all transitions between them do not change either. Furthermore, the drift velocities of electrons in the channels do not depend on the LL index.

The adiabatic approximation becomes increasingly inadequate when the distance to the edge becomes of the order of a few magnetic lengths. In order to proceed, we need to specify the shape of the edge potential. It obviously depends on the details of the interface and is affected by the presence of the surface states, any space charge accumulation which tends to further sharpen the potential profile [30], etc. In order to obtain quantitative results we take the simplest nonadiabatic potential: the hard wall condition [8,31], or a step in  $\Phi(y)$  at  $y = 0$ , which for a high enough potential barrier means that for a given LL index  $n$  and  $x$  component of momentum  $k$ ,  $\chi_{nk}(0) = 0$  and  $\chi_{nk}(y \rightarrow \infty) = 0$ . Although obviously an idealization of any realistic boundary, the hard wall condition captures the main physical effects of the nonadiabatic interface, namely asymmetry of the wave functions near the boundary (see the Supplemental Material [28]), nonequidistant eigenenergies  $E_{nk}$  of the edge states as shown in Fig. 3, modified polarization selection rules which increasingly favor  $y$  polarization as the states are pressed to the edge, and inversion symmetry breaking which leads to nonzero permanent dipole moments and modified LL number  $n$  selection rules: the transitions with  $n$  changing by 2 become allowed in the electric dipole approximation. Finally, the electron drift velocity in the state  $|nk\rangle$ , i.e., the diagonal matrix element of the velocity operator, becomes  $n$  and  $k$  dependent and has a

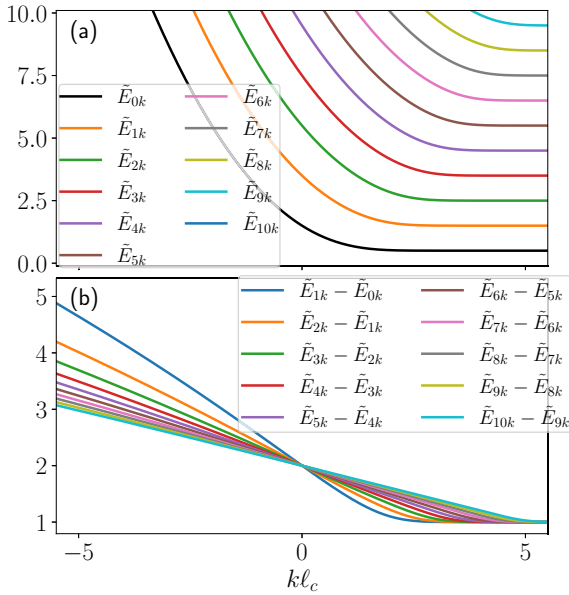


FIG. 3. (a) Numerically obtained energy eigenvalues (normalized with  $\hbar\omega_c$ ) from Eq. (1) in the presence of hard wall at  $y = 0$  for the first 11 eigenvalues corresponding to  $n = 0, 1, \dots, 10$  respectively, as a function of the center of cyclotron rotation  $y_k/\ell_c = k\ell_c$ . (b) Difference between consecutive energy eigenvalues as a function of  $k\ell_c$ . Here  $\bar{E}_{nk} \equiv E_{nk}/\hbar\omega_c$ .

standard form (see Appendix B for derivation):

$$\langle \hat{v}_x \rangle_{nk} = \frac{1}{\hbar} \frac{\partial E_{nk}}{\partial k}. \quad (2)$$

Note that this expression does not depend on the specific form of the eigenstates  $\psi_{nk}(x, y)$ ; moreover, Eq. (2) does not depend on any assumptions about the nonuniformity scale of the potential  $\Phi(y)$  in comparison with the magnetic length  $\ell_c$ .

We will consider the observational consequences of these effects one by one below, keeping the derivation details and lengthy formulas in the Appendix. Before using a numerical solution of Eq. (1) with a hard wall potential to calculate the optical response, we point out two approximate analytical solutions of Eq. (1) for a hard-wall boundary condition  $\Phi(y > 0) = 0$  and  $\chi_{nk}(0) = 0$ .

### A. Asymptotic solution for $n \gg 1$

In this case, analytical solutions can be obtained within the quasiclassical approximation [32]. For  $y_k > \sqrt{2E/(m\omega_c^2)}$ , the quasiclassical solution of Eq. (1) corresponds to two turning points in the region  $y > 0$  (one at  $y > y_k > 0$  and another at  $y_k > y > 0$ ), for which  $E = m\omega_c^2(y - y_k)^2/2$ . In this case the solution obeys the Bohr-Sommerfeld quantization rule, which for Eq. (1) corresponds to standard eigenenergies  $E_n = \hbar\omega_c(n + 1/2)$ . For  $y_k < \sqrt{2E/(m\omega_c^2)}$  there is one turning point at  $y > y_k > 0$  and another one due to reflection from the wall at  $y = 0$ . Denoting the turning point at  $y \neq 0$  as  $y^*$ , we write the quasi-classical solution of Eq. (1) as

$$\chi_{nk}(y) = \frac{1}{N_{nk}\sqrt{q_{nk}}} \cos\left(\int_y^{y^*} dy q_{nk}(y) - \frac{\pi}{4}\right), \quad (3)$$

where  $\hbar q_{nk}(y) = \sqrt{2m[E_{nk} - m\omega_c^2(y - y_k)^2/2]}$  and  $q_{nk}(y^*) = 0$ . Here  $N_{nk}$  is the normalization factor. Taking into account the boundary condition on the ideally reflecting wall, i.e.,  $\chi_{nk}(0) = 0$ , we obtain the transcendental equation for the eigenenergies as

$$E_{nk} = \frac{2\pi(n + 3/4)\hbar\omega_c}{2\beta_{nk} - \sin(2\beta_{nk})}, \quad (4)$$

with  $\cos(\beta_{nk}) = -\hbar k/\sqrt{2mE_{nk}}$ . For  $y_k \propto k > 0$  and  $1 - \hbar k/\sqrt{2mE_{nk}} \ll 1$ , we have  $\beta_{nk} \rightarrow \pi$ , i.e.,  $E_{nk} = (n + 3/4)\hbar\omega_c$ . As we see, the energy is increased by  $\hbar\omega_c/4$  as compared to the LL in the bulk. This is the result of changing boundary conditions from a smooth effective potential to a hard wall. For  $y_k = 0$ ,  $\beta_{nk} = \pi/2$ , which gives  $E_{nk} = (2n + 3/2)\hbar\omega_c$ . Here the energy is raised by more than a factor of 2 as compared to the LLs in the bulk. For  $y_k < 0$ , one can find the asymptotic solution for  $E_{nk} \gg n\hbar\omega_c$ , which corresponds to the large wave number limit,  $|k|\ell_c \gg \sqrt{n}$ . In this case we need to have  $\beta_{nk} - \sin(2\beta_{nk})/2 \ll 1$ , i.e.,  $\beta_{nk} \rightarrow 0$ . Denoting  $\varepsilon_k = \hbar^2 k^2/(2m)$ , we obtain

$$E_{nk} \approx \varepsilon_k + \left[\frac{3\pi}{2}\hbar\omega_c\left(n + \frac{3}{4}\right)\right]^{2/3} \varepsilon_k^{1/3}, \quad (5)$$

implying that the energies increase and the distance between LLs grows non-equidistantly. This already suggests that for a vertical wall or for any non-adiabatic potential one can realize resonant optical transitions between edge states without causing resonant absorption between bulk LLs.

### B. Solution for any $n$ but large wave numbers $k$

Let us denote  $V(y) = m\omega_c^2(y - y_k)^2/2$ . Under the condition  $V'(y)|_{y=y^*} - V'(y)|_{y=0} \ll V'(y)|_{y=0}$ , where  $E = V(y^*)$ , and for  $\xi = (2|k|/\ell_c^2)^{1/3}(y - (E - \varepsilon_k)/(\hbar\omega_c|k|))$ , Eq. (1) can be transformed to

$$\frac{\partial^2 \chi}{\partial \xi^2} - \xi \chi = 0.$$

We can choose our solution as the Airy function  $\text{Ai}(\xi)$ , which goes to zero for  $\xi \rightarrow \infty$  and satisfies the boundary condition  $\chi(y = 0) = 0$ , with the corresponding eigenenergies

$$E_{nk} = \varepsilon_k + (\hbar\omega_c)^{2/3} \varepsilon_k^{1/3} |\xi_n|, \quad (6)$$

where  $\xi_n$  are zeros of the Airy function, i.e.,  $\text{Ai}(\xi_n) = 0$ ,  $n = 0, 1, 2, \dots$ . Here  $\xi_0$  is the zero with value closest to  $\xi = 0$ , and their values  $|\xi_n|$  increase with increasing  $n$ . One can verify that Eq. (6) is valid as long as  $|k|\ell_c \gg \sqrt{n}$ . The eigenfunctions  $\chi_{nk}(y)$  corresponding to eigenenergies  $E_{nk}$  are defined in the interval  $0 \leq y < \infty$  as

$$\chi_{nk}(y) = \frac{1}{\tilde{N}_{nk}} \text{Ai}\left(y\left(\frac{2|k|}{\ell_c^2}\right)^{1/3} + \xi_n\right), \quad (7)$$

with  $\tilde{N}_{nk}$  being the normalization factor which is given as,

$$\tilde{N}_{nk}^2 = \left(\frac{\ell_c^2}{2|k|}\right)^{1/3} \int_{\xi_n}^{\infty} \text{Ai}^2(\xi) d\xi. \quad (8)$$

The dispersion of eigenenergies (6) has the similar structure to those in the previous subsection, even though the former does not rely on  $n$  being large.

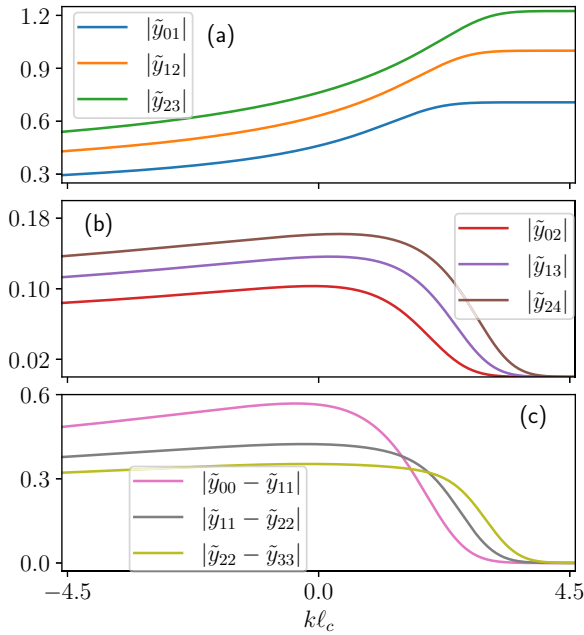


FIG. 4. Magnitude of the normalized dipole matrix elements as a function of the center of the cyclotron rotation  $y_k/l_c = k l_c$  for transitions (a)  $n \rightarrow n + 1$ , (b)  $n \rightarrow n + 2$ , and (c) the difference of intra-LL dipole elements. Here  $\tilde{y}_{ij} \equiv y_{ik;jk}/l_c$ .

### C. Exact numerical solution for eigenstates and dipole matrix elements

Finally, we compute the eigenvalues and the eigenfunctions for Eq. (1) numerically using Numerov's algorithm. Fig. 3 shows the eigenenergies for the first 11 LLs as a function of  $y_k/l_c = k l_c$ , and the energy differences between neighboring eigenvalues. It demonstrates not only the bending of flat LLs of the bulk states near the edge of the sample, but also the fact that the optical transitions become increasingly nonequidistant and move to higher energies as compared to the transitions between bulk LLs. This agrees qualitatively with photovoltage measurements in terahertz spectroscopy of edge states [33,34]. It is also worth pointing out strong inhomogeneous broadening of the inter-LL optical transitions.

The dipole matrix elements and selection rules are modified drastically in the presence of the boundary, mostly due to inversion symmetry breaking. In the electric dipole approximation, the general expression for carrier velocity along  $\hat{x}$  direction which includes both diagonal ( $n = m$ ) and off-diagonal ( $n \neq m$ ) elements is

$$\langle nk | \hat{v}_x | mk' \rangle = \delta_{kk'} \omega_c (y_k \delta_{nm} - y_{nk;mk}), \quad (9)$$

with  $y_{nk;mk} = \langle nk | y | mk \rangle$ . In the bulk, vertical transitions between  $m$ th and  $n$ th LLs obey the following selection rule,

$$\frac{y_{nk;mk}}{l_c} = \delta_{n,m+1} \sqrt{\frac{n}{2}}. \quad (10)$$

This simple relation, however, does not hold for edge states. In Fig. 4, we plot the dipole elements as a function of the center of the cyclotron rotation  $y_k/l_c = k l_c$  for transitions involving the first several LLs. The panel (a) shows that the dipole elements deviate from Eq. (10) as  $y_k$  approaches the

edge. At the same time, previously forbidden transitions  $n \rightarrow n + 2$  are activated, as shown in panel (b). Furthermore, the permanent, intra-LL dipole matrix elements differ from their bulk values as well (panel (c)), such that their differences between consecutive LLs change from zero to finite values. Both effects are a consequence of inversion symmetry breaking and lead to large second-order nonlinearity in the electric-dipole approximation, as we will see below.

### III. QUANTUM THEORY OF THE PHOTON ABSORPTION

Since one of the most interesting possibilities offered by the optical field is to excite a single electron into a given edge state, we need a fully quantized theory of fermions in a QH sample interacting with a quantized electromagnetic field. We will derive both the probability of a single photon absorption and the absorbance of a classical field.

It is convenient to describe the quantum state of electrons in terms of occupation numbers of  $|nk\rangle = \chi_{nk}(y) e^{ikx}$  states, for example  $|\dots 1_{nk} \dots 0_{n'k'} \dots\rangle$ , where  $1_{nk}$  and  $0_{n'k'}$  are occupied and unoccupied states. Fermionic annihilation and creation operators are acting on these states in the usual way:  $\hat{a}_{nk} |\dots 1_{nk} \dots\rangle = |\dots 0_{nk} \dots\rangle$  and  $\hat{a}_{nk}^\dagger |\dots 0_{nk} \dots\rangle = |\dots 1_{nk} \dots\rangle$ . The electron Hamiltonian is then  $\hat{H}_e = \sum_{n,k} E_{nk} \hat{a}_{nk}^\dagger \hat{a}_{nk}$ .

The Hamiltonian and the operator of the vector potential of the EM field incident on the sample are

$$\hat{H}_{\text{ph}} = \sum_{\mathbf{v}, \mathbf{q}} \hbar \omega_{\mathbf{v}\mathbf{q}} \left( \hat{b}_{\mathbf{v}\mathbf{q}}^\dagger \hat{b}_{\mathbf{v}\mathbf{q}} + \frac{1}{2} \right), \quad (11)$$

$$\hat{\mathbf{A}} = \sum_{\mathbf{v}, \mathbf{q}} \sqrt{\frac{2\pi c^2 \hbar}{V \omega_{\mathbf{q}}}} (\mathbf{e}_{\mathbf{v}\mathbf{q}} \hat{b}_{\mathbf{v}\mathbf{q}} e^{i\mathbf{q}\mathbf{r}} + \mathbf{e}_{\mathbf{v}\mathbf{q}}^* \hat{b}_{\mathbf{v}\mathbf{q}}^\dagger e^{-i\mathbf{q}\mathbf{r}}), \quad (12)$$

where  $\hat{b}_{\mathbf{v}\mathbf{q}}$  and  $\hat{b}_{\mathbf{v}\mathbf{q}}^\dagger$  are the photon annihilation and creation operators acting on the photon Fock states  $|n_{\mathbf{v}\mathbf{q}}\rangle$ ,  $\omega_{\mathbf{q}} = c|\mathbf{q}|$ ,  $V$  is the quantization volume with periodic boundary conditions, and  $\mathbf{e}_{\mathbf{v}\mathbf{q}}$  is the polarization vector such that  $\mathbf{q} \cdot \mathbf{e}_{\mathbf{v}\mathbf{q}} = 0$ . The total Hamiltonian is

$$\hat{H} = \hat{H}_e + \hat{H}_{\text{ph}} + \hat{H}_{\text{int}}, \quad (13)$$

where the interaction Hamiltonian  $\hat{H}_{\text{int}} = -\frac{1}{c} \hat{\mathbf{j}} \cdot \hat{\mathbf{A}}$  and the current operator is  $\hat{\mathbf{j}} = -e\hat{\mathbf{v}}$ . From the general relation  $\mathbf{v}_{nk;n'k'} = -i\omega_{nk;n'k'} \mathbf{r}_{nk;n'k'}$ , where  $\hbar\omega_{nk;n'k'} = E_{nk} - E_{n'k'}$ , we can express the current matrix elements through the dipole matrix elements discussed in the previous section:

$$\mathbf{j}_{nk;n'k'} = \mathbf{j}_{nk;n'k'} \delta_{kk'}, \quad (14)$$

$$(j_x)_{nk;n'k} = e\omega_c y_{nk;n'k}, \quad (15)$$

$$(j_y)_{nk;n'k} = ie\omega_{nk;n'k} y_{nk;n'k}, \quad (16)$$

which results in the modified polarization selection rules:

$$(j_x)_{nk;n'k} + i \frac{\omega_c}{\omega_{nk;n'k}} (j_y)_{nk;n'k} = 0. \quad (17)$$

As follows from Eq. (17) and Fig. 3(b), for electron states near the edge the transition frequency  $\omega_{nk;n'k}$  becomes several times larger than  $\omega_c$  and therefore the  $y$  component of the

current matrix element becomes significantly larger than the  $x$ -component.

Now consider the normal incidence of the radiation on the Hall sample, when  $\mathbf{q} = q\mathbf{z}_0$ , and take the field quantization volume as a ray bundle of volume  $V = l_x l_y l_z$ . For our purpose it is sufficient to consider only one spatial mode at frequency  $\omega_q = cq$  and polarization  $\mathbf{e}_q$ . It is straightforward to generalize it to a multimode wave-packet. As a result, in the rotating-wave approximation (RWA) the interaction Hamiltonian becomes

$$\hat{H}_{\text{int}} = - \sum_{k, n > n'} \sqrt{\frac{2\pi\hbar}{V\omega_q}} (\mathbf{e}_q \cdot \mathbf{j}_{nk;n'k} \hat{b}_q \hat{a}_{kn}^\dagger \hat{a}_{kn'} + \text{H.c.}).$$

As an initial state of electrons we take

$$\Psi_e(0) = \prod_{\{nk\}_{\text{occ}}} \hat{a}_{kn}^\dagger |0_e\rangle$$

where  $|0_e\rangle$  is the vacuum state of the electron system, and  $\{nk\}_{\text{occ}}$  denotes occupied states. The values of  $n$  change from  $n = 0$  to  $n = n_F$  where  $n_F$  is the index of the highest occupied LL in the bulk, whereas the values of  $k$  change up to  $k_{nF}$ , for which  $E_{nk} = E_F$ , where  $E_F$  is the Fermi energy. An initial single-photon state of the field is

$$\Psi_{\text{ph}}(0) = \hat{b}_q^\dagger |0_p\rangle,$$

where  $|0_p\rangle$  is the vacuum state of the field. We seek the solution of the Schrödinger equation as

$$\Psi(t) = C_q(t) \Psi_{\text{ph}}(0) \Psi_e(0) + \sum_{\{n'k\}_{\text{occ}, n}} C_{n'nk}(t) |0_p\rangle \hat{a}_{nk}^\dagger \hat{a}_{n'k} \Psi_e(0). \quad (18)$$

This ansatz includes an initial state and all possible states resulting from the absorption of a single photon, all with their unknown time-dependent probability amplitudes. In Eq. (18) the summation is performed only over the indices  $n, n'$  and  $k$  which at the initial moment of time correspond to occupied states  $|n'k\rangle$  and empty states  $|nk\rangle$ . At  $t = 0$  we have  $C_q(0) = 1$  and  $C_{n'nk}(0) = 0$ . The Schrödinger equation leads to linear equations for the complex amplitudes  $C_q(t)$  and  $C_{n'nk}(t)$ , that are similar to those for a quantum field interacting with an inhomogeneously broadened ensemble of two-level quantum emitters [35]. This analogy works because all transitions are assumed to conserve the electron quasimomentum. We then proceed to solve the equations for the probability amplitudes within the stochastic Schrödinger's equation (SSE) approach [35], which is equivalent to the master equation approach in the Lindblad approximation. Solving them, one can obtain a complete quantum dynamic of light-matter interaction in our system. In particular, in the perturbative linear regime we obtain the absorption probability per unit time and per given transition  $n' \rightarrow n$  as

$$\begin{aligned} \mathcal{A}_{n' \rightarrow n} &= \sum_k \frac{d}{dt} |C_{n'nk}(t)|^2 \\ &= \sum_k \frac{4\pi |\mathbf{j}_{nk;n'k} \cdot \mathbf{e}_q^*|^2}{\hbar\omega(l_x l_y l_z)} \frac{\gamma (F_{n'k}^{(0)} - F_{nk}^{(0)})}{\gamma^2 + (\omega_{nk;n'k} - \omega)^2}, \end{aligned} \quad (19)$$

where  $\gamma$  is the homogeneous broadening of inter-LL transitions determined by disorder-induced scattering and  $F_{jk}^{(0)} = (1 + e^{(E_{jk} - E_F)/(k_B T)})^{-1}$  is the Fermi distribution function at temperature  $T$ . For small  $\gamma$  as compared to the inhomogeneous broadening of transitions between edge states, the Lorentzian in Eq. (19) becomes the delta function  $\pi\delta(\omega_{nk;n'k} - \omega)$  and one recovers the Fermi's golden rule expression. In the case of a finite  $\gamma$ , stochastic noise terms appear in the equations for complex amplitudes according to the stochastic Schrödinger equation approach [35], but this will not affect the linear absorption probability.

The summation over  $k$  can be replaced by integration,  $\sum_k \rightarrow g_s \frac{L_x}{2\pi} \int dk$ , where we also added the spin degeneracy factor  $g_s$ . Here  $L_x$  is the sample length (quantization length of electron states) in  $x$ -direction along the edge. The total absorption probability is obtained by adding the contributions from all LL transitions,  $\mathcal{A}_{\text{tot}} = \frac{l_z}{c} \sum_{n, n'} \mathcal{A}_{n' \rightarrow n}$ . Here we also converted the probability per unit time into the total dimensionless probability of absorbing a photon by multiplying the former by the photon pulse duration  $\Delta t \approx l_z/c$ . Defined this way, the photon absorption probability will also describe the dimensionless absorbance of the classical monochromatic wave by a 2D system. Here we obviously assumed a rectangular temporal profile of the pulse for simplicity. Propagation of single-photon pulses of an arbitrary shape involves a bit more algebra and can be found, e.g., in Ref. [36].

The resulting expression depends on the geometric parameter  $\frac{L_x}{l_x l_y}$ , which can be written as a dimensionless factor

$$f = \frac{L_x l_c}{l_x l_y}.$$

This factor measures the overlap of an incident radiation beam with electron states in the  $(x, y)$  plane, and it was assumed in the derivation that the area of the photon beam is larger than the sample area. Therefore, the value of  $f$  is expected to be much smaller than 1, especially due to the ratio  $l_c/l_y$  which is always small. Indeed, for a GaAs/AlGaAs quantum well with the conduction band effective mass of  $0.067m_0$  [37] and in a magnetic field  $B = 1$  T, we have  $\hbar\omega_c \approx 1.7$  meV and  $l_c \approx 26$  nm. If we want to focus incident THz radiation tightly on one edge of the sample in order to bring the overlap closer to 1, one should illuminate a metal tip or fabricate a metallic nanoantenna along the sample edge.

In order to show universal, geometry-independent absorbance spectra, we normalize the absorbance by this geometric overlap factor, namely

$$\mathcal{A}(\omega) = \frac{\mathcal{A}_{\text{tot}}}{f} = \frac{1}{f} \frac{l_z}{c} \sum_{n, n'} \mathcal{A}_{n' \rightarrow n}. \quad (20)$$

The resulting spectra  $\mathcal{A}(\omega)$  of absorbance (or single-photon absorption probability) are shown in Figs. 5(a) and 5(c) for the case of  $y$ -polarized radiation. The shaded regions under the black curve show the contributions of individual transitions between neighboring LLs; the range of these transitions in momentum space is shown in the insets, with colors matching the shaded regions in the main figure. The salient feature of the total absorbance spectra is the existence of the sharp peaks at frequencies where the contributions from two different transitions overlap. The overlaps exist in the region

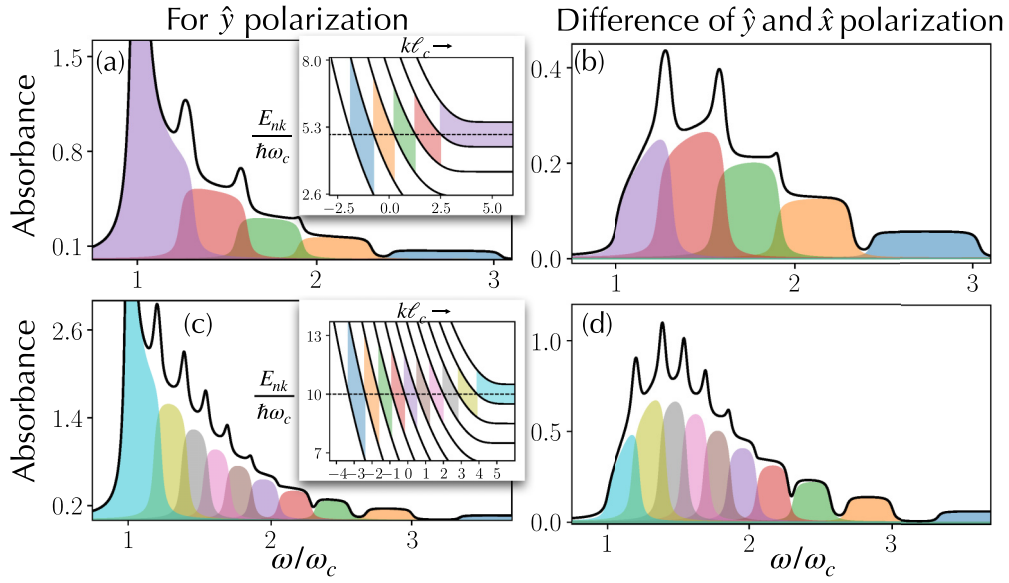


FIG. 5. Normalized absorbance spectra given by Eq. (20) (solid black line) of  $\hat{y}$ -polarized photons for (a) Fermi energy above the fifth LL and (c) Fermi energy above the tenth LL. (b) and (d) show the difference between the absorbance of  $\hat{y}$  and  $\hat{x}$  polarization for the same Fermi levels ( $x$ -polarized absorbance subtracted from  $y$  polarized one). The shaded colored regions under the black curves show the contributions of individual transitions between the neighboring LLs. The insets in (a) and (c) show the regions of phase space which contribute to the absorption of photons for each pair of neighboring LLs. The colors of shades in the inset match those in the main figure for each panel. Other parameters are  $\gamma = 0.02 \omega_c$  and temperature  $T = 0$ .

of momenta  $k > 0$  and frequencies  $\omega_c < \omega < 2\omega_c$ , as one can also see from the spread of transition energies in Fig. 3(b). For higher frequencies and for the states closer to the edge ( $k < 0$ ) the overlaps disappear and the peaks in Fig. 5 turn into dips, as is also clear from Fig. 3(b) where the order of transition energies between neighboring LLs gets inverted upon crossing  $k = 0$ . These peaks and dips provide a clear spectroscopic signature of individual edge states. Moreover, they also provide an opportunity of exciting nonequilibrium carriers into a given edge state and then observe a corresponding change in the edge-state interferometry. Due to a large spectral detuning from the bulk transitions at  $\omega = \omega_c$  this is possible without destroying the QH effect conditions in the bulk of the sample.

One detrimental factor that could possibly affect the edge state spectroscopy, especially with broadband pulses, is the presence of a strong peak at  $\omega = \omega_c$  due to the bulk state transition  $n_F \rightarrow n_F + 1$ . However, this peak can be subtracted out in the measurements of difference between absorbance in  $x$ - and  $y$ -polarizations, as shown in Figs. 5(b) and 5(d). Here we make use of the fact that near the edge the  $x$ - and  $y$ -components of transition matrix elements become increasingly different, with a much stronger  $y$ -component, as follows from Eq. (17). Thus, difference measurements will get rid of the bulk peak and may result in easier observable peaks and dips for edge states.

As one can see from Fig. 5, the magnitude of absorbance peaks normalized by the geometric factor  $f$  is of the order of 1-3. Therefore, the fraction of light absorbed in individual peaks is essentially the above factor  $f$  measuring the overlap of the incident radiation with the sample. While there is no doubt that  $f \ll 1$ , one needs to keep it large enough to ensure that the absorption is detectable. As an example, consider a QH sample of size  $L_x \sim L_y \sim 10 \mu\text{m}$ . If the incident radiation

is focused on the whole area of the sample, e.g., by a mask or a metallic antenna, then  $l_{x,y} \sim L_{x,y} \sim 10 \mu\text{m}$  and  $f \sim 2.6 \times 10^{-3}$ , where we took the value of  $\ell_c \approx 26 \text{ nm}$  in GaAs for  $B = 1 \text{ T}$ . So, the photon absorption probability, or two-dimensional absorbance, will be around  $3f \sim 0.8 \%$  at the highest peak position which has the value around  $\mathcal{A}(\omega) \simeq 3$  according to Fig. 5(c). This is a small but measurable value.

One can get higher absorbances by focusing incident radiation into a smaller area with a nanotip or a nanoantenna. For  $l_x < L_x$  the absorption probability becomes independent on  $L_x$  and the geometric factor in Eq. (20) is simply  $f = \ell_c/l_y$ . By focusing into the spot size of  $\sim 30 \text{ nm}$ , one can get an absorption probability approaching 1.

One can also estimate the magnitude of absorbance analytically by taking the limit  $\gamma \rightarrow 0$  which converts Eq. (19) into the one given the Fermi's Golden Rule, with the delta-function in the integrand describing energy conservation. Performing integration in  $k$ , we obtain

$$\frac{l_z}{c} \mathcal{A}_{n' \rightarrow n} = f \frac{2\pi |\mathbf{j}_{nk;n'k} \cdot \mathbf{e}_q^*|^2}{\hbar \omega c \ell_c \partial_k \omega_{nk;n'k}} \Big|_{\omega_{nk;n'k} = \omega}, \quad (21)$$

where we also took the population difference equal to 1. Using the expression for energy dispersion provided in the Eq. (5) (or Eq. (6)), we find  $\partial_k \omega_{nk;n'k} = 2\omega_{nk;n'k}/(3k)$ . For a  $y$ -polarized field we have  $|\mathbf{j}_{nk;n'k} \cdot \mathbf{e}_q^*|^2 = e^2 \omega_{nk;n'k}^2 |y_{nk;n'k}|^2$ . This gives

$$\frac{l_z}{c} \mathcal{A}_{n' \rightarrow n} = f \frac{3\pi \alpha}{\ell_c} |y_{nk;n'k}|^2 k \Big|_{\omega_{nk;n'k} = \omega}, \quad (22)$$

where  $\alpha$  is the fine structure constant,  $k$  scales as  $\omega_{nk;n'k}^{3/2}$ , and the momentum dependence of  $|y_{nk;n'k}|^2$  can be extracted from Fig. 4. For example, if we take the wavenumber of

the initial state at the Fermi level,  $k \approx k_F \approx \frac{1}{\ell_c} \sqrt{2n_F + 1}$ , the absorbance due to the transition between these LLs is

$$\frac{l_z}{c} \mathcal{A}_{n' \rightarrow n} \approx f 3\pi \alpha \sqrt{2n_F + 1} \frac{|y_{nk_F, n'k_F}|^2}{\ell_c^2}. \quad (23)$$

#### IV. GENERATION OF DC CURRENT BY OPTICAL RECTIFICATION

The DC current carried by chiral edge states in QH effect experiments is proportional to the diagonal elements of the density matrix,

$$\mathcal{J}_0 = -\frac{e}{L_x} \sum_{n,k} (v_x)_{nk;nk} \rho_{nk;nk}^{(0)}. \quad (24)$$

The net current from both edges is zero, but it becomes nonzero if a DC voltage  $\Delta V$  is applied. Indeed, using Eq. (24) together with Eq. (2), one can find out that in equilibrium, the difference between the currents along opposite edges  $\Delta \mathcal{J}_0 = \frac{e^2 n_F}{2\pi \hbar} \Delta V$ , where  $n_F$  is the number of filled LLs in the bulk.

However, inversion symmetry breaking for edge states gives rise to the possibility of generating the DC or quasi-DC current by an *optical* field through the second-order process of the optical rectification, which becomes allowed in the electric dipole approximation. In order to support the net current only one edge needs to be illuminated; otherwise the contributions of two opposite edges will still cancel each other.

This optically driven DC current is due to the off-diagonal elements of the density matrix,

$$\mathcal{J}_{dc} = \frac{e^2 B}{L_x m c} \sum_{n \neq m} \sum_k y_{nk;mk} \rho_{mk;nk}. \quad (25)$$

The density matrix elements are found by solving the master equation,

$$\frac{\partial \rho_{nm}}{\partial t} + \frac{i}{\hbar} \sum_v (H_{nv} \rho_{vm} - \rho_{nv} H_{vm}) = 0, \quad (26)$$

to which we will add phenomenological relaxation terms  $\gamma \rho_{nm}$ . Here  $H_{\alpha\beta} = \delta_{\alpha\beta} E_\alpha + V_{\alpha\beta}(t)$  and  $\alpha, \beta$  represent the quantum state comprising the Landau level index and the momentum. The light-matter interaction Hamiltonian in electric-dipole approximation is  $\hat{V}(t) = ey(\mathcal{E}e^{-i\omega t} + \mathcal{E}^*e^{i\omega t})$ , where we assume the field to be classical in this section. Since all optical transitions are vertical in the electric-dipole approximation, we suppressed the momentum index for simplicity, such that  $y_{ik;jk} \rightarrow y_{ij}$  and  $\rho_{ik;jk} \rightarrow \rho_{ij}$ . The momentum index has to be restored when integrating over  $k$  in Eq. (25).

We proceed by expanding the elements of the density matrix in the perturbative series with respect to the interaction Hamiltonian,

$$\frac{\partial \rho_{nm}^{(j+1)}}{\partial t} = -i\omega_{nm} \rho_{nm}^{(j+1)} - \frac{i}{\hbar} \sum_v (V_{nv} \rho_{vm}^{(j)} - \rho_{nv}^{(j)} V_{vm}), \quad (27)$$

with  $n$  and  $m$  denoting the quantum states corresponding to Landau level indices  $n$  and  $m$  respectively. We are only interested in the terms up to the second order in the optical field.

The linear in  $\mathcal{E}$  term yields

$$\rho_{\beta\alpha}^{(1)} = -\frac{e}{\hbar} \frac{y_{\beta\alpha} (\rho_{\alpha\alpha}^{(0)} - \rho_{\beta\beta}^{(0)})}{\omega_{\beta\alpha} - \omega - i\gamma} \mathcal{E} e^{-i\omega t}, \quad (28)$$

where  $\rho_{\alpha\beta}^{(1)} = (\rho_{\beta\alpha}^{(1)})^*$ .

From Eq. (25) and taking into account the structure of the perturbative solution, it is clear that there are two types of contributions to the DC current at zero frequency, i.e.,  $\propto |\mathcal{E}|^2$ . One type of the terms in Eq. (25) scales as  $y_{n;(n+2)} \rho_{(n+2);n}^{(2)}$ . They are enabled by nonzero dipole matrix elements  $y_{n;(n+2)}$  of the transitions which change the LL index by 2, i.e.,  $n \rightarrow n+2$ . The second group of the terms scales as  $y_{n;(n+1)} \rho_{(n+1);n}^{(2)}$  where  $\rho_{(n+1);n}^{(2)} \propto (y_{(n+1);(n+1)} - y_{n;n})$ . As one can see from Fig. 4, both  $y_{n;(n+2)}$  and  $(y_{(n+1);(n+1)} - y_{n;n})$  are only nonzero for electron states close to the edge, when the center of the cyclotron rotation  $y_k$  is within several magnetic lengths  $\ell_c$  from the edge.

The second-order nonlinear density matrix elements contributing to the DC current satisfy the equations of motion

$$\begin{aligned} & \frac{\partial \rho_{n;(n-1)}^{(2)}}{\partial t} + i\omega_{n;(n-1)} \rho_{n;(n-1)}^{(2)} \\ &= -\frac{ie}{\hbar} \mathcal{F}(t) [y_{n;(n-2)} \rho_{(n-2);(n-1)}^{(1)} - y_{(n-2);(n-1)} \rho_{n;(n-2)}^{(1)} \\ & \quad + y_{n;(n+1)} \rho_{(n+1);(n-1)}^{(1)} - y_{(n+1);(n-1)} \rho_{n;(n+1)}^{(1)} \\ & \quad + (y_{n;n} - y_{(n-1);(n-1)}) \rho_{n;(n-1)}^{(1)}], \end{aligned} \quad (29)$$

$$\begin{aligned} & \frac{\partial \rho_{(n+1);(n-1)}^{(2)}}{\partial t} + i\omega_{(n+1);(n-1)} \rho_{(n+1);(n-1)}^{(2)} \\ &= -\frac{ie}{\hbar} \mathcal{F}(t) [y_{(n+1);n} \rho_{n;(n-1)}^{(1)} - y_{n;(n-1)} \rho_{(n+1);n}^{(1)} \\ & \quad + (y_{(n+1);(n+1)} - y_{(n-1);(n-1)}) \rho_{(n+1);(n-1)}^{(1)}], \end{aligned} \quad (30)$$

where we have defined  $\mathcal{F}(t) = \mathcal{E}e^{-i\omega t} + \mathcal{E}^*e^{i\omega t}$ . Time-independent solution to these equations under illumination with a monochromatic field gives rise to a large number of terms contributing to the DC current, which grows rapidly with increasing doping. For convenience, in Appendix C below we list the density matrix elements that contribute to the rectification current for the Fermi level  $E_F = 3\hbar\omega_c$  between  $n=2$  and  $n=3$  bulk LLs, chosen to make plots in Fig. 6. In Fig. 6 the red curve shows the rectification current normalized by the conventional ‘‘diagonal’’ DC current (24) and by the dimensionless factor

$$\zeta = \frac{e^2 |\mathcal{E}|^2 \ell_c^2}{\hbar^2 \omega_c^2} \quad (31)$$

as a function of the optical field frequency. The current is a sum of the above two contributions,  $\mathcal{J}_{dc}^{(I)}$  and  $\mathcal{J}_{dc}^{(II)}$ , given by

$$\mathcal{J}_{dc}^{(I/II)} = \frac{e^2 B}{mc} \int \frac{dk}{2\pi} J^{(I/II)}, \quad (32)$$

where

$$J^{(I)} = y_{01} \rho_{10}^{(2)} + y_{12} \rho_{21}^{(2)} + y_{23} \rho_{32}^{(2)} + \text{c.c.}, \quad (33)$$

$$J^{(II)} = y_{02} \rho_{20}^{(2)} + y_{13} \rho_{31}^{(2)} + y_{24} \rho_{42}^{(2)} + \text{c.c.} \quad (34)$$

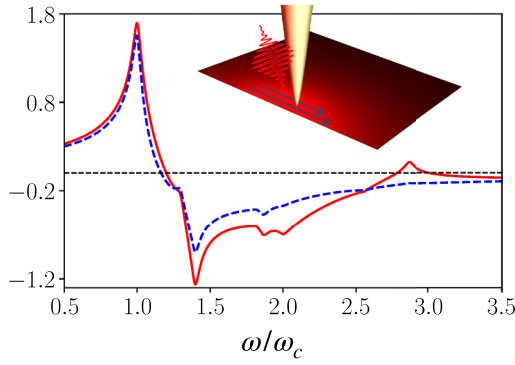


FIG. 6. Nonlinear DC current resulting from second-order optical rectification process, as a function of the normalized optical field frequency. The calculations included the first five Landau levels for chemical potential  $E_F = 3\hbar\omega_c$ . Red curve: The electric dipole contribution to the nonlinear current from Eq. (32),  $\frac{\mathcal{J}_{\text{dc}}^{(I)} + \mathcal{J}_{\text{dc}}^{(II)}}{\zeta \mathcal{J}_0}$ , normalized by the “diagonal” DC current  $\mathcal{J}_0$  from Eq. (24) and factor  $\zeta$  from Eq. (31). Blue dashed curve: Beyond electric-dipole contribution to the nonlinear current,  $\frac{\mathcal{J}_{\text{dc}}^{(III)} + \mathcal{J}_{\text{dc}}^{(IV)}}{\zeta_{\text{grad}} \mathcal{J}_0}$ , normalized by  $\mathcal{J}_0$  and factor  $\zeta_{\text{grad}}$  from Eq. (35).

The expressions for the second-order density matrix elements are given in Appendix C.

The main peak at the cyclotron frequency in Fig. 6 is due to the  $n = 2 \rightarrow n = 3$  transition near the edge. With increasing optical frequency, the term  $(E_{3k} - E_{2k})/\hbar - \omega$  flips sign and consequently we observe a negative peak in the plot. Additional kinks are due to activation/deactivation of various transitions. They are going to be smeared by finite temperature effects and/or increased scattering.

Since the normalized nonlinear current in Fig. 6 is of the order of 1, the dimensional current magnitude is a fraction  $\zeta$  of the conventional edge current (24). The factor  $\zeta$  is essentially the Rabi frequency squared of incident light normalized to the cyclotron frequency squared. When  $\zeta$  becomes of the order of 1, population transfer effects between the LLs in the bulk become important even despite the detuning from the bulk inter-LL resonance. This could create bulk conductance across the sample and destroy the QH effect. Therefore, to maintain the QH effect conditions in the bulk, it is desirable to keep  $\zeta \ll 1$ . The optimal situation to observe or utilize the nonlinear rectification current would be to illuminate one edge of the sample under zero DC bias conditions, when the net conventional current is zero.

### A. Beyond electric-dipole approximation

Yet another second-order nonlinear optical contribution to the rectified DC current originates from the spatial nonuniformity of the electric field of the incident radiation, i.e., beyond the electric-dipole approximation. In the lowest order, the light-matter interaction Hamiltonian becomes

$$\hat{V}(t) = e \left[ \left( y\mathcal{E} + \frac{y^2}{2} \partial_y \mathcal{E} \right) e^{-i\omega t} + \left( y\mathcal{E} + \frac{y^2}{2} \partial_y \mathcal{E} \right)^* e^{i\omega t} \right].$$

This gives rise to the following additional matrix elements contributing to the rectification current,

$$V_{(n+2);n} = \frac{e}{2} (y^2)_{(n+2);n} (\partial_y \mathcal{E} e^{-i\omega t} + \partial_y \mathcal{E}^* e^{i\omega t}),$$

$$V_{(n+1);n} = \frac{e}{2} (y^2)_{(n+1);n} (\partial_y \mathcal{E} e^{-i\omega t} + \partial_y \mathcal{E}^* e^{i\omega t}).$$

Solving the density matrix equations in the second order of the field as in the previous subsection, we obtain additional contributions to the density matrix elements. For example, the factor  $y_{12}y_{20}\mathcal{E}^*\mathcal{E}$  in the first term in  $\rho_{10}^{(2)}$  in Appendix C is modified as  $y_{12}y_{20}\mathcal{E}^*\mathcal{E} + y_{12}y_{20}^2\mathcal{E}^*\partial_y\mathcal{E}/2 + y_{12}^2y_{20}\mathcal{E}\partial_y\mathcal{E}^*/2$ , and similarly for other terms.

We denote the resulting contributions as  $J^{III}$  and  $J^{IV}$  in the spirit of Eq. (33) and Eq. (34), respectively, and calculate the resulting rectification current  $\mathcal{J}_{\text{dc}}^{(III)} + \mathcal{J}_{\text{dc}}^{(IV)}$  similarly to Eq. (32). It is shown as a blue dashed curve in Fig. 6. The current is normalized by the conventional “diagonal” DC current (24) and by the factor

$$\zeta_{\text{grad}} = \frac{e^2 \ell_c^3 \partial_y |\mathcal{E}|^2}{\hbar^2 \omega_c^2} \quad (35)$$

proportional to the gradient of the optical field intensity. With this normalization, the optical rectification current is close in magnitude to the one obtained in electric dipole approximation and shown as a red curve. Note, however, that the normalization factor in the denominator contains the optical field intensity gradient  $\ell_c \partial_y |\mathcal{E}|^2$  which is much smaller than  $|\mathcal{E}|^2$ , unless the optical field is focused to the size of the order of  $\ell_c$ , i.e., tens of nm, by using a nanotip or nanoantenna at the sample edge as sketched in the inset to Fig. 6. Without nanofocusing, the electric-dipole current is greater in magnitude by the factor  $\sim \frac{|\mathcal{E}|^2}{\ell_c \partial_y |\mathcal{E}|^2}$ .

As was pointed out in [29], the ponderomotive force proportional to the gradient of the optical field intensity can modify the transport and lead to MIRO-ZRS like phenomena even in the limit of classical electron motion and neglecting any nonadiabaticity near the edge. The interplay between edge-induced classical magnetoplasmon effects and quantum nonadiabaticity will make an interesting topic for future studies.

## V. CONCLUSIONS

In conclusion, we have demonstrated the feasibility of optical spectroscopy and selective coherent optical control of chiral edge state populations and currents under the conditions of the integer QH effect. The physical mechanism enabling this selective control involves inversion symmetry breaking and violation of adiabaticity for electron states near the edge. As a result, optical transitions between edge states have significantly different transition energies and polarization selection rules as compared to the bulk of the sample. This enables selective excitation of a specific edge channel with single quasiparticle sensitivity without disturbing the rest of the sample.

The 2D absorbance reveals characteristic peaks corresponding to various edge state resonances at frequencies significantly higher than the bulk cyclotron transition. A large fraction of incident light within the illuminated area of the

sample can be absorbed. The overall absorption probability of single photons depends on their spatial overlap with the edge state area which can be enhanced through nanofocusing with a tip or nanoantenna.

Furthermore, inversion symmetry breaking near the sample boundary enables strong second-order optical nonlinearity in the electric dipole approximation, resulting in efficient optical rectification of incident radiation and direct optical driving of a quasi-DC current in edge states. The predicted optical effects can be used to study or control edge currents by optical means and to control the interference pattern in QH interference experiments.

While the calculations in this paper were performed for nonrelativistic electron dispersion in semiconductor quantum wells, one should expect a qualitatively similar strategy of selective optical spectroscopy of edge states to be applicable to graphene samples. The quantitative results will be different due to the presence of two types of terminations in graphene. The results will be reported elsewhere.

Another natural extension of this work is to investigate the optical control of edge currents under fractional QH effect conditions. We anticipate that this study will attract attention of both the QH and optical communities, fostering interesting collaborative experiments.

#### ACKNOWLEDGMENTS

This work has been supported in part by the Air Force Office for Scientific Research Grant No. FA9550-21-1-0272 and National Science Foundation Award No. 1936276. M.T. acknowledges the support by the Center for Integration in Science of the Ministry of Aliya and Integration, Israel.

#### APPENDIX A: ELECTRON STATES IN ADIABATIC APPROXIMATION

For the reader's convenience, here we summarize the results for electron states in the adiabatic approximation, when the electric potential  $\Phi(y)$  varies much slower than the magnetic length. For a magnetic field,  $\vec{B} = B\hat{z}$  we choose the vector potential of the form  $\vec{A} = -yB\hat{x}$ , which yields the single-electron Hamiltonian

$$H = \frac{1}{2m} \left( p_x - \frac{eBy}{c} \right)^2 + \frac{p_y^2}{2m} - e\Phi, \quad (\text{A1})$$

where  $m$  is the electron mass. Since there is no explicit  $x$  dependence, we can seek the wavefunction as

$$\psi(x, y) = e^{ikx} \chi(y), \quad (\text{A2})$$

for which the Schrödinger equation yields

$$\frac{\partial^2 \chi}{\partial y^2} + \frac{2m}{\hbar^2} \left[ E + e\Phi(y) - \frac{1}{2} m \omega_c^2 (y - y_k)^2 \right] \chi(y) = 0. \quad (\text{A3})$$

where we have defined the cyclotron frequency,  $\omega_c = eB/(mc)$ , the position of the center of the cyclotron rotation  $y_k = k\ell_c^2$ , and the magnetic length  $\ell_c = \sqrt{\hbar/(eB)}$ .

In the adiabatic approximation, the potential  $\Phi(y)$  is varying slowly near the edge,  $\Phi(y) \approx \Phi(y_k) + (y - y_k)$

$(\partial_y \Phi(y)|_{y=y_k})$ . The particle energies are

$$E_{nk} = \left( n + \frac{1}{2} \right) \hbar \omega_c - e \Phi \left( y_k + \frac{c \partial_y \Phi(y)|_{y=y_k}}{\omega_c B} \right) + \frac{m}{2} \left( \frac{c \partial_y \Phi(y)|_{y=y_k}}{B} \right)^2. \quad (\text{A4})$$

The term  $\frac{c \partial_y \Phi(y)|_{y=y_k}}{\omega_c B}$  in the right-hand side of Eq. (A4) is the shift of the center of the cyclotron rotation with respect to the initial point  $y_k$  under the action of the electric field  $E_y \approx -\partial_y \Phi(y)|_{y=y_k}$ . The last term on the right-hand side of Eq. (A4) is the kinetic energy of the drift motion in crossed  $E$  and  $B$  fields.

The eigenfunctions become

$$\chi_{nk}(y) = \frac{e^{-(y-y_k - c \partial_y \Phi(y)|_{y=y_k}/(\omega_c B))^2 / (\sqrt{2} \ell_c)^2}}{\sqrt{2^n n! \sqrt{\pi} \ell_c}} \times \mathcal{H}_n \left( \frac{y}{\ell_c} - \frac{y_k}{\ell_c} - \frac{c}{\ell_c} \frac{\partial_y \Phi(y)|_{y=y_k}}{\omega_c B} \right), \quad (\text{A5})$$

where  $n$  is the LL index and  $\mathcal{H}_n$  is a Hermite polynomial. In this case, while the energies of the LLs increase towards the edge, the energy separation between them does not change as compared to the bulk states, and the dipole matrix elements of all transitions between them do not change either. Furthermore, the drift velocity of electrons along the edge does not depend on the LL index:

$$\langle \hat{v}_x \rangle_k = -\frac{c}{B} \partial_y \Phi(y)|_{y=y_k}. \quad (\text{A6})$$

#### APPENDIX B: ELECTRON DENSITY FLUX FOR AN ARBITRARY POTENTIAL

It is interesting that the electron density flux and drift velocity can be found for an arbitrary potential  $\Phi(y)$ , provided Eq. (1) allows a finite solution corresponding to a certain discrete spectrum of  $E_{nk}$  and a set of eigenfunctions of the form  $\psi_{nk}(x, y) = e^{ikx} \chi_{nk}(y)$ , where  $\chi_{nk}(y)|_{y \rightarrow \pm\infty} \rightarrow 0$ ,  $\int dx dy \psi_{nk}^*(x, y) \psi_{mk'}(x, y) = \delta_{nm} \delta_{kk'}$ . To prove this, we introduce the operator of two-dimensional electron density for the  $n$ th LL,  $\hat{N}_n(x, y) = \hat{\Psi}^\dagger(x, y) \hat{\Psi}(x, y)$  where the field operators are given in the second-quantized form:  $\hat{\Psi}(x, y) = \sum_k \psi_{nk}(x, y) \hat{a}_{nk}$ ,  $\hat{\Psi}^\dagger = \sum_k \psi_{nk}^*(x, y) \hat{a}_{nk}^\dagger$  with the annihilation and creation operators  $\hat{a}_{nk}$  and  $\hat{a}_{nk}^\dagger$  respectively. The operator of two-dimensional spatial electron density is then

$$\hat{N}_n(x, y) = \sum_{k, k'} \chi_{nk'}^*(y) \chi_{nk}(y) e^{i(k-k')x} \hat{\rho}_{nk;nk'}, \quad (\text{B1})$$

where  $\hat{\rho}_{nk;nk'} = \hat{a}_{nk}^\dagger \hat{a}_{nk'}$ . The same result can be obtained by using the transition operator  $\hat{\rho}_{nk;nk'} = |nk\rangle \langle nk'|$ . The operator  $\hat{\rho}_{nk;nk'}$  obeys the Heisenberg equation,

$$\frac{\partial \hat{\rho}_{nk;nk'}}{\partial t} = -\frac{i}{\hbar} (E_{nk} - E_{nk'}) \hat{\rho}_{nk;nk'}. \quad (\text{B2})$$

If the fermions are interacting with classical electromagnetic fields, the Heisenberg operator  $\hat{\rho}_{nk;nk'}$ , after averaging over the initial state of the system, becomes the matrix element of a standard density matrix  $\rho_{nk;nk'}$ . The general expression for the probability flux of the electron density can be expressed

through the Wigner function, defined as

$$\hat{\mathcal{W}}_n(x, y, K) = \sum_{\kappa} \psi_{n(K-\kappa/2)}^*(x, y) \psi_{n(K+\kappa/2)}(x, y) \times \hat{\rho}_{n(K+\kappa/2);n(K-\kappa/2)},$$

where  $k - k' = \kappa$ ,  $(k + k')/2 = K$ . The Wigner function  $\hat{\mathcal{W}}_n(x, y, K)$  determines both the operator of spatial density,

$$\sum_K \hat{\mathcal{W}}_n(x, y, K) = \hat{N}_n(x, y), \quad (\text{B3})$$

and the distribution over momenta,

$$\int dx dy \hat{\mathcal{W}}_n(x, y, K)|_{K=k} = \hat{\rho}_{nk;nk}. \quad (\text{B4})$$

It follows from Eq. (B2) that

$$\frac{\partial \hat{\rho}_{n(K+\kappa/2);n(K-\kappa/2)}}{\partial t} = -\frac{i}{\hbar} (E_{n(K+\kappa/2)} - E_{n(K-\kappa/2)}) \times \hat{\rho}_{n(K+\kappa/2);n(K-\kappa/2)}. \quad (\text{B5})$$

Suppose that we have a well-localized state in  $k$  so that  $\delta k \ll k$  (a narrow spectrum in  $k$  means narrow localization along  $y$  near the edge). In this case we have  $E_{n(K+\kappa/2)} -$

$E_{n(K-\kappa/2)} \approx \kappa \partial_k E_{nk}|_{k=K}$ . Then from Eq. (B5) and taking into account Eqs. (B3) and (B4) one can obtain

$$\frac{\partial \hat{\mathcal{W}}_n(x, y, K)}{\partial t} + \frac{1}{\hbar} \frac{\partial E_{nk}}{\partial k} \Big|_{k=K} \frac{\partial \hat{\mathcal{W}}_n(x, y, K)}{\partial x} = 0. \quad (\text{B6})$$

For a quadratic spectrum of the type  $E_{nk} = E_{n0} + \alpha_n k^2$  Eq. (B6) is exact and does not require a narrow spectrum.

Using Eqs. (B6) and (B3), one can obtain

$$\frac{\partial \hat{N}_n(x, y)}{\partial t} + \frac{1}{\hbar} \frac{\partial E_{nk}}{\partial k} \frac{\partial \hat{N}_n(x, y)}{\partial x} = 0 \quad (\text{B7})$$

where  $k$  is the central value of the given narrow spectrum. From Eq. (B7) one obtains the expression for the observed particle velocity in the state  $|nk\rangle$ , i.e., the diagonal matrix element of the velocity operator, which has a standard form:

$$\langle \hat{v}_x \rangle_{nk} = \frac{1}{\hbar} \frac{\partial E_{nk}}{\partial k}. \quad (\text{B8})$$

Note that this expression coincides with the one obtained from the solution (A5) for a uniform electric field but it does not depend on the specific form of the eigenstates  $\psi_{nk}(x, y)$ ; furthermore, Eq. (B8) does not depend on any assumptions about the nonuniformity scale of the potential  $\Phi(y)$  in comparison with the magnetic length  $\ell_c$ .

### APPENDIX C: SECOND-ORDER NONLINEAR DENSITY MATRIX ELEMENTS

For the reader's convenience, we provide below the list of second-order nonlinear density matrix elements that contribute to the optical rectification current in the electric-dipole approximation for our chosen value of the Fermi level,  $E_F = 3\hbar\omega_c$ :

$$\begin{aligned} \frac{\rho_{10}^{(2)}}{e^2 |\mathcal{E}|^2 / \hbar^2} &= \frac{y_{12} y_{20} \Delta \rho_{02}^{(0)}}{\omega_{10} (\Delta_{20} - i\gamma)} - \frac{y_{20} y_{12} \Delta \rho_{12}^{(0)}}{\omega_{10} (\Delta_{21} + i\gamma)} - \frac{(y_{00} - y_{11}) y_{10} \Delta \rho_{01}^{(0)}}{\omega_{10} (\Delta_{10} - i\gamma)}, \\ \frac{\rho_{21}^{(2)}}{e^2 |\mathcal{E}|^2 / \hbar^2} &= \frac{y_{20} y_{01} \Delta \rho_{01}^{(0)}}{\omega_{21} (\Delta_{10} + i\gamma)} - \frac{y_{01} y_{20} \Delta \rho_{02}^{(0)}}{\omega_{21} (\Delta_{20} - i\gamma)} + \frac{y_{23} y_{31} \Delta \rho_{13}^{(0)}}{\omega_{21} (\Delta_{31} - i\gamma)} - \frac{y_{31} y_{23} \Delta \rho_{23}^{(0)}}{\omega_{21} (\Delta_{32} + i\gamma)} - \frac{(y_{11} - y_{22}) y_{21} \Delta \rho_{12}^{(0)}}{\omega_{21} (\Delta_{21} - i\gamma)}, \\ \frac{\rho_{32}^{(2)}}{e^2 |\mathcal{E}|^2 / \hbar^2} &= \frac{y_{31} y_{12} \Delta \rho_{12}^{(0)}}{\omega_{32} (\Delta_{21} + i\gamma)} - \frac{y_{12} y_{31} \Delta \rho_{13}^{(0)}}{\omega_{32} (\Delta_{31} - i\gamma)} + \frac{y_{34} y_{42} \Delta \rho_{24}^{(0)}}{\omega_{32} (\Delta_{42} - i\gamma)} - \frac{y_{42} y_{34} \Delta \rho_{34}^{(0)}}{\omega_{32} (\Delta_{43} + i\gamma)} - \frac{(y_{22} - y_{33}) y_{32} \Delta \rho_{23}^{(0)}}{\omega_{32} (\Delta_{32} - i\gamma)}, \\ \frac{\rho_{43}^{(2)}}{e^2 |\mathcal{E}|^2 / \hbar^2} &= \frac{y_{42} y_{23} \Delta \rho_{23}^{(0)}}{\omega_{43} (\Delta_{32} + i\gamma)} - \frac{y_{23} y_{42} \Delta \rho_{24}^{(0)}}{\omega_{43} (\Delta_{42} - i\gamma)}, \\ \frac{\rho_{20}^{(2)}}{e^2 |\mathcal{E}|^2 / \hbar^2} &= \frac{y_{21} y_{10} \Delta \rho_{01}^{(0)}}{\omega_{20} (\Delta_{10} - i\gamma)} - \frac{y_{10} y_{21} \Delta \rho_{12}^{(0)}}{\omega_{20} (\Delta_{21} - i\gamma)} - \frac{(y_{00} - y_{22}) y_{20} \Delta \rho_{02}^{(0)}}{\omega_{20} (\Delta_{20} - i\gamma)}, \\ \frac{\rho_{31}^{(2)}}{e^2 |\mathcal{E}|^2 / \hbar^2} &= \frac{y_{32} y_{21} \Delta \rho_{12}^{(0)}}{\omega_{31} (\Delta_{21} - i\gamma)} - \frac{y_{21} y_{32} \Delta \rho_{23}^{(0)}}{\omega_{31} (\Delta_{32} - i\gamma)} - \frac{(y_{11} - y_{33}) y_{31} \Delta \rho_{13}^{(0)}}{\omega_{31} (\Delta_{31} - i\gamma)}, \\ \frac{\rho_{42}^{(2)}}{e^2 |\mathcal{E}|^2 / \hbar^2} &= \frac{y_{43} y_{32} \Delta \rho_{23}^{(0)}}{\omega_{42} (\Delta_{32} - i\gamma)} - \frac{(y_{22} - y_{44}) y_{42} \Delta \rho_{24}^{(0)}}{\omega_{42} (\Delta_{42} - i\gamma)}. \end{aligned}$$

Here  $\Delta \rho_{\alpha\beta}^{(0)} = (\rho_{\alpha\alpha}^{(0)} - \rho_{\beta\beta}^{(0)})$  is the equilibrium population difference and  $\Delta_{\alpha\beta} = \omega_{\alpha\beta} - \omega$ .

[1] Edited by R. E. Prange and S. M. Girvin, *The Quantum Hall Effect* (Springer, New York, 1987).

[2] B. I. Halperin, Quantized Hall conductance, current-carrying edge states, and the existence of extended states in a two-dimensional disordered potential, *Phys. Rev. B* **25**, 2185 (1982).

[3] A. H. MacDonald and P. Štředa, Quantized Hall effect and edge currents, *Phys. Rev. B* **29**, 1616 (1984).

[4] N. Pascher, C. Rössler, T. Ihn, K. Ensslin, C. Reichl, and W. Wegscheider, Imaging the conductance of integer and fractional quantum Hall edge states, *Phys. Rev. X* **4**, 011014 (2014).

- [5] A. Marguerite, J. Birkbeck, A. Aharon-Steinberg, D. Halbertal, K. Bagani, I. Marcus, Y. Myasoedov, A. K. Geim, D. J. Perello, and E. Zeldov, Imaging work and dissipation in the quantum Hall state in graphene, *Nature (London)* **575**, 628 (2019).
- [6] T. Johnsen, C. Schattauer, S. Samaddar, A. Weston, M. J. Hamer, K. Watanabe, T. Taniguchi, R. Gorbachev, F. Libisch, and M. Morgenstern, Mapping quantum Hall edge states in graphene by scanning tunneling microscopy, *Phys. Rev. B* **107**, 115426 (2023).
- [7] G. Li, A. Luican-Mayer, D. Abanin, L. Levitov, and E. Y. Andrei, Evolution of Landau levels into edge states in graphene, *Nat. Commun.* **4**, 1744 (2013).
- [8] T. Patlatiuk, C. P. Scheller, D. Hill, Y. Tserkovnyak, G. Barak, A. Yacoby, L. N. Pfeiffer, K. W. West, and D. M. Zumbühl, Evolution of the quantum Hall bulk spectrum into chiral edge states, *Nat. Commun.* **9**, 3692 (2018).
- [9] S. Kim, J. Schwenk, D. Walkup, Y. Zeng, F. Ghahari, S. T. Le, M. R. Slot, J. Berwanger, S. R. Blankenship, K. Watanabe, T. Taniguchi, F. J. Giessibl, N. B. Zhitenev, C. R. Dean, and J. A. Stroscio, Edge channels of broken-symmetry quantum Hall states in graphene visualized by atomic force microscopy, *Nat. Commun.* **12**, 2852 (2021).
- [10] B. J. van Wees, L. P. Kouwenhoven, C. J. P. M. Harmans, J. G. Williamson, C. E. Timmering, M. E. I. Broekaart, C. T. Foxon, and J. J. Harris, Observation of zero-dimensional states in a one-dimensional electron interferometer, *Phys. Rev. Lett.* **62**, 2523 (1989).
- [11] C. de C. Chamon, D. E. Freed, S. A. Kivelson, S. L. Sondhi, and X. G. Wen, Two point-contact interferometer for quantum Hall systems, *Phys. Rev. B* **55**, 2331 (1997).
- [12] Y. Ji, Y. Chung, D. Sprinzak, M. Heiblum, D. Mahalu, and H. Shtrikman, An electronic Mach-Zehnder interferometer, *Nature (London)* **422**, 415 (2003).
- [13] S. B. Chung and M. Stone, Proposal for reading out anyon qubits in non-abelian  $\nu = 12/5$  quantum Hall state, *Phys. Rev. B* **73**, 245311 (2006).
- [14] A. Stern and B. I. Halperin, Proposed experiments to probe the non-Abelian  $\nu = 5/2$  quantum Hall state, *Phys. Rev. Lett.* **96**, 016802 (2006).
- [15] D. E. Feldman and A. Kitaev, Detecting non-abelian statistics with an electronic Mach-Zehnder interferometer, *Phys. Rev. Lett.* **97**, 186803 (2006).
- [16] Y. Zhang, D. T. McClure, E. M. Levenson-Falk, C. M. Marcus, L. N. Pfeiffer, and K. W. West, Distinct signatures for Coulomb blockade and Aharonov-Bohm interference in electronic Fabry-Pérot interferometers, *Phys. Rev. B* **79**, 241304 (2009).
- [17] A. Stern, B. Rosenow, R. Ilan, and B. I. Halperin, Interference, Coulomb blockade, and the identification of non-abelian quantum Hall states, *Phys. Rev. B* **82**, 085321 (2010).
- [18] C. Déprez, L. Veyrat, H. Vignaud, G. Nayak, K. Watanabe, T. Taniguchi, F. Gay, H. Sellier, and B. Sacépé, A tunable Fabry-Pérot quantum Hall interferometer in graphene, *Nat. Nanotechnol.* **16**, 555 (2021).
- [19] D. E. Feldman and B. I. Halperin, Robustness of quantum Hall interferometry, *Phys. Rev. B* **105**, 165310 (2022).
- [20] J. Nakamura, S. Liang, G. C. Gardner, and M. J. Manfra, Direct observation of anyonic braiding statistics, *Nat. Phys.* **16**, 931 (2020).
- [21] Y. Ronen, T. Werkmeister, D. Haie Najafabadi, A. T. Pierce, L. E. Anderson, Y. J. Shin, S. Y. Lee, Y. H. Lee, B. Johnson, K. Watanabe, T. Taniguchi, A. Yacoby, and P. Kim, Aharonov-Bohm effect in graphene-based Fabry-Pérot quantum Hall interferometers, *Nat. Nanotechnol.* **16**, 563 (2021).
- [22] J. Nakamura, S. Liang, G. C. Gardner, and M. J. Manfra, Fabry-Pérot interferometry at the  $\nu = 2/5$  fractional quantum Hall state, *Phys. Rev. X* **13**, 041012 (2023).
- [23] F. Appugliese, J. Enkner, G. L. Paravicini-Bagliani, M. Beck, C. Reichl, W. Wegscheider, G. Scalari, C. Ciuti, and J. Faist, Breakdown of topological protection by cavity vacuum fields in the integer quantum Hall effect, *Science* **375**, 1030 (2022).
- [24] I. A. Dmitriev, A. D. Mirlin, D. G. Polyakov, and M. A. Zudov, Nonequilibrium phenomena in high Landau levels, *Rev. Mod. Phys.* **84**, 1709 (2012).
- [25] A. Kriisa, R. L. Samaraweera, M. S. Heimbeck, H. O. Everitt, C. Reichl, W. Wegscheider, and R. G. Mani, Cyclotron resonance in the high mobility GaAs/AlGaAs 2D electron system over the microwave, mm-wave, and terahertz bands, *Sci. Rep.* **9**, 2409 (2019).
- [26] T. Herrmann, Z. D. Kvon, I. A. Dmitriev, D. A. Kozlov, B. Jentzsch, M. Schneider, L. Schell, V. V. Bel'kov, A. Bayer, D. Schuh, D. Bougeard, T. Kuczmik, M. Oltcher, D. Weiss, and S. D. Ganichev, Magnetoresistance oscillations induced by high-intensity terahertz radiation, *Phys. Rev. B* **96**, 115449 (2017).
- [27] M. L. Savchenko, A. Shuvaev, I. A. Dmitriev, S. D. Ganichev, Z. D. Kvon, and A. Pimenov, Demonstration of high sensitivity of microwave-induced resistance oscillations to circular polarization, *Phys. Rev. B* **106**, L161408 (2022).
- [28] See Supplemental Material at <http://link.aps.org/supplemental/10.1103/PhysRevB.110.085405> for boundary effects on the wavefunctions corresponding to the first three Landau levels.
- [29] S. A. Mikhailov, Theory of microwave-induced zero-resistance states in two-dimensional electron systems, *Phys. Rev. B* **83**, 155303 (2011).
- [30] D. B. Chklovskii, B. I. Shklovskii, and L. I. Glazman, Electrostatics of edge channels, *Phys. Rev. B* **46**, 4026 (1992).
- [31] W. N. Mei and Y. C. Lee, Harmonic oscillator with potential barriers-exact solutions and perturbative treatments, *J. Phys. A: Math. Gen.* **16**, 1623 (1983).
- [32] L. D. Landau and E. M. Lifshitz, *Quantum Mechanics: Non-Relativistic Theory* (Elsevier Science, 1981).
- [33] R. Merz, F. Keilmann, R. J. Haug, and K. Ploog, Nonequilibrium edge-state transport resolved by far-infrared microscopy, *Phys. Rev. Lett.* **70**, 651 (1993).
- [34] C. Notthoff, K. Rachor, D. Heitmann, and A. Lorke, Terahertz photoresponse of a quantum Hall edge-channel diode, *Phys. Rev. B* **80**, 205320 (2009).
- [35] M. Tokman, A. Behne, B. Torres, M. Erukhimova, Y. Wang, and A. Belyanin, Dissipation-driven formation of entangled dark states in strongly coupled inhomogeneous many-qubit systems in solid-state nanocavities, *Phys. Rev. A* **107**, 013721 (2023).
- [36] M. Tokman, J. K. Verma, J. Bohrer, and A. Belyanin, Maximally efficient biphoton generation by single photon decay in nonlinear quantum photonic circuits, *Phys. Rev. Lett.* **131**, 233802 (2023).
- [37] I. Lo, W. C. Mitchel, R. E. Perrin, R. L. Messham, and M. Y. Yen, Two-dimensional electron gas in GaAs/Al<sub>1-x</sub>Ga<sub>x</sub>As heterostructures: Effective mass, *Phys. Rev. B* **43**, 11787 (1991).